

Chiral Self-Assembly of Cellulose Nanocrystals is Driven by Crystallite Bundles

*Thomas G. Parton, Gerda van de Kerkhof, Aurimas Narkevicius, Johannes Haataja, Richard M. Parker, Bruno Frka-Petecic, Silvia Vignolini**

Yusuf Hamied Department of Chemistry, University of Cambridge, Lensfield Road, Cambridge CB2 1EW, United Kingdom

*sv319@cam.ac.uk

Abstract

Cellulose nanocrystals (CNCs) are bio-sourced colloidal particles able to self-assemble into chiral photonic structures, but the origin of their mesophase chirality remains unclear. Moreover, the lack of statistically significant characterisation of the particle size and shape make it challenging to apply predictive models. In this work, nanoparticle shape metrology was implemented to track morphological changes induced by ultrasonication, enabling quantitative comparison of individual particle morphology and ensemble behaviour both in suspensions and cast films. The chiral nematic pitch was found to rely on the presence of crystallite bundles, a ubiquitous feature of CNC suspensions not previously associated with their chiral self-assembly. The bundles have an effective helical twisting power of $\beta = 4 \mu\text{m}^{-1}$ when modelled as chiral dopants, analogous to those used in molecular liquid crystals. These results indicate that CNC crystallites bundles are the missing link in the hierarchical transfer of chirality from the molecular to colloidal level.

Introduction

The chiral self-assembly of nanoscale building blocks is a fascinating example of emergence of large-scale structure from the properties of individual sub-units (1, 2). However, understanding the transfer of chirality across length-scales from the nanoscale to the macroscopic system remains a significant challenge, despite its importance for unlocking the potential of self-organised nanomaterials. In many self-assembled colloidal systems, such as rod-like viruses, amyloid fibrils and DNA origami filaments, the emergence of mesophase chirality has been associated with the uniform twisted morphology or chiral bending properties of assembling sub-units (3–6). In contrast, for bio-sources rod-shaped particles such as cellulose nanocrystals (CNCs), the origin of the chirality transfer from individual particles to their mesophase remains elusive, despite intensive research on cellulose nanomaterials over the past few decades (7).

CNCs form a stable left-handed chiral nematic phase under a range of experimental conditions, enabling their use as chiral scaffolds or structurally coloured photonic films (8–10). CNC mesophase chirality is often attributed to the morphology of individual CNC *crystallites* (i.e. the elongated crystalline units within a single CNC particle), which have a propensity to twist about their long axis, a property that ultimately arises from the molecular chirality of individual D-glucose monosaccharides (7, 11, 12). However, the majority of CNC particles lack a consistent twisted morphology, being composed of irregular laterally-bound *bundles* of rod-like crystallites and exhibiting substantial variation in size and shape (13–16). The contribution of bundles to the chiral self-assembly of CNCs is rarely discussed, with an implicit assumption that they make no particular contribution to the self-assembly process.

In this work, we demonstrate that bundles of crystallites, which are ubiquitous in CNC suspensions, are intrinsically related to the chirality of CNC self-assembly. By applying ultrasonication to tune the size and shape of the CNCs and using nanoparticle shape metrology, we establish quantitative relationships between colloidal liquid crystalline behaviour and the morphological distribution of CNC particles. We demonstrate that the increase in chiral nematic pitch with sonication dose, corresponding to a red-shift in the colour of the resulting CNC photonic films, cannot be explained solely by the chirality of individual crystallites or by changes in electrostatic interactions. Instead, we show that CNC bundles are crucial for the transfer of chirality from individual CNC crystallites to the chiral nematic phase. These results suggest that the concept of a chiral dopant, established for molecular liquid crystals, can be directly applied to understand the behaviour of this colloidal liquid crystal system.

Results

Tuning the colour of CNC photonic films with sonication

The chiral self-assembly of CNCs can be used to produce photonic films by drying a chiral nematic suspension to preserve its helicoidal structure (17). Previous studies on CNC self-assembly have focussed on relating the visual appearance of films, most notably colour, to the physical and chemical properties of the initial suspension (8). For example, increasing the ionic strength of the suspension enhances the chiral interaction between CNCs, resulting in a smaller chiral nematic pitch that corresponds to a blue-shifted colour in the final film (14). In contrast, the application of high-intensity ultrasound by tip sonication (hereafter referred to as simply “sonication”) is known to increase the pitch in suspension, resulting in a red-shift in the corresponding film (18).

Although the pitch increase with sonication is well-established and routinely used in the CNC community, the origin of this effect is still debated (8). Sonication breaks apart CNC particles and thus increases the ionic conductivity of the suspension by liberating trapped ions. It has therefore been proposed that the

pitch increase arises from an expansion of the effective CNC particle size due to these released ions (18). However, this argument appears to contradict the expected behaviour of charged colloids, where increasing ionic strength is found to decrease the effective particle volume by reducing the thickness of the electric double layer. Moreover, it is expected that the chiral interactions between CNCs derive from their physical shape rather than dispersion forces, as CNCs can also form a chiral nematic phase when electrostatic and van der Waals interactions are suppressed by suspending the CNCs in index-matching apolar solvents (19). These observations suggest that sonication-induced changes to particle morphology (i.e. size and shape) are the origin of the change in chiral nematic pitch.

To explore the effect of sonication on CNC self-assembly, CNC suspensions were prepared at a wide range of sonication doses (0-12 kJ/mL, Materials and Methods). Note that the sonication dose is expressed as thermally dissipated energy per suspension volume (J/mL), which was found to be a consistent dose unit under different experimental conditions, unlike nominal energy per dry mass of CNC (J/gCNC), which is more commonly used in the nanocellulose literature (see fig. S1 and associated discussion). To rule out the influence of released ions, the suspensions were extensively dialysed against deionised water. The CNC surface charge and zeta potential were measured after dialysis and showed no significant change with sonication (table S1).

The sonicated CNC suspensions were cast in Petri dishes to produce photonic films with structural colour across the visible spectrum, as shown in **Fig. 1A**. Unsonicated suspensions (0 kJ/mL) produced films with a weak bluish colour, attributed to scattering from the disordered structure, while high sonication doses (>2 kJ/mL) resulted in films with no visible colour.

The morphological changes induced by sonication are evident from transmission electron microscopy, as shown in **Fig. 1B-1D**. At low sonication dose, many CNCs take the form of bundles, or elongated aligned clusters of laterally-bound crystallites, as exemplified in **Fig. 1E**. It is important to clarify that bundles are a native component of CNC suspensions and are not produced by aggregation of crystallites during TEM sample preparation, as validated by the presence of bundles in cryoTEM images (fig. S5). Sonication breaks apart bundles and liberates the constituent crystallites to be suspended freely. While size parameters such as the average hydrodynamic diameter (**Fig. 1F**) or particle cross-section (fig. S4) decrease with sonication, the breakdown of bundles into crystallites is a more subtle morphological change that is not evident from ensemble measurements, or even from measuring simple nanoparticle size parameters such as length and width.

To quantitatively address the increase in pitch with sonication, the pitch was measured by two methods: indirectly, from the peak reflection wavelength using optical spectroscopy, and directly, from cross-sectional scanning electron microscopy (SEM) images (**Fig. 1G**, fig. S2 and fig. S3). In the visible range, the observed pitch increase is consistent with the colour change in **Fig. 1A**. Cross-sectional SEM also reveals that the pitch diverges in the near-infrared reflection range, with no pitch observed for the film at the highest sonication dose (12 kJ/mL), suggesting that excessive sonication impedes the chiral self-assembly of the CNCs.

If the mesophase chirality of CNC suspensions arose directly from the chirality of individual crystallites, the pitch would be expected to remain unchanged or even decrease when the crystallites were liberated from bundles. As the opposite trend is observed in **Fig. 1G**, we hypothesised that the bundles play an essential role in the transfer of chirality from the crystallites to the chiral nematic phase.

Revealing the 3D morphological changes by nanoparticle shape metrology

To better characterise the variation in CNC morphology induced by sonication, we performed an in-depth analysis using the outlines of CNCs obtained from TEM images (Materials and Methods). This nanoparticle metrology approach allows us to capture, in a statistically significant way, the size and shape distribution of individual nanoparticles at each sonication stage

CNCs are typically slender elongated particles, with a length considerably greater than their width, as exemplified in **Fig. 2A**. While the acicular shape of CNCs makes it appropriate to approximate their dimensions to ideal shapes such as rectangles or ellipses, capturing the full outline of the particles enables advanced statistical analysis of a variety of size and shape parameters. For instance, the length and width of CNCs can be defined as the dimensions of the smallest box that encloses the particle outline (**Fig. 2B**), denoted the box length L_b and box width W_b respectively. While L_b is a good approximation of the particle length, W_b is an upper bound and therefore over-estimates the actual particle width. A more appropriate alternative is the area-equivalent (AE) width $W_{eq} = A/L_b$, where A is the area enclosed by the particle outline. The AE width more accurately captures the average width of irregular elongated particles than the box width, as illustrated in **Fig. 2B**

The CNC particle cross-section is approximately rectangular, with a thickness limited by the fundamental dimensions of individual CNC crystallite units (**Fig. 2C**). The thickness of CNC particles, which is not accessible in TEM images, can be measured by complementary methods such as atomic force microscopy (AFM) or wide angle X-ray scattering and indicate that most CNCs are a single crystallite in thickness (20).

The morphological changes induced by sonication can be studied by looking at the changes in size and shape distributions, obtained from histograms of experimental data. For example, **Fig. 2D** shows distributions for the box length at a range of sonication doses (indicated by the values on the left-hand side of the plot). The mean box length (indicated by the circles in **Fig. 2D**) decreases with sonication, in agreement with previous reports, and other common size parameters (e.g. area, perimeter, box width) show a similar overall decrease with sonication dose (fig. S6) (18).

Plotting the distributions side-by-side as shown in **Fig. 2D** facilitates comparison between samples and the direct observation of various statistical features. For instance, it is clear that the box length distribution is well-described by a log-normal distribution, which appears as a symmetric normal peak when plotted on a log scale. The apparent width of the peak decreases slightly with sonication, indicating a mild decrease in length polydispersity ($\sigma_L/\mu_L \approx 0.5$).

In contrast, the AE width distributions exhibit multimodal behaviour, with a low-width peak emerging at higher sonication doses (**Fig. 2E**). This peak, centred around 7 nm, can be attributed to individual CNC crystallites. Plotting the experimental TEM histograms provides further evidence of the discretisation of CNC equivalent width. Furthermore, the AE width distribution becomes substantially narrower with increasing sonication, indicating a considerable decrease in width polydispersity with sonication.

Theoretical studies on elongated particles have demonstrated that the aspect ratio is important for understanding their mesophase self-assembly (21). However, calculating the aspect ratio for CNCs is non-trivial due to their lath-like 3D morphology. The apparent 2D aspect ratio based on particle length and width in TEM (e.g. $\alpha_{app} = L_b/W_{eq}$) is therefore inappropriate to model the colloidal behaviour of CNCs and can be misleading, with no clear correlation between α_{app} and sonication dose observed (fig. S6). To account for the non-circular cross-section of CNC particles, an effective 3D aspect ratio can be defined:

$$\alpha_{\text{eff}} = L_b / \sqrt{W_{\text{eq}} T} \quad (2)$$

where T is the thickness of a single CNC crystallite. Here T was obtained by atomic force microscopy (AFM) and found to have a mean value of 4.8 nm (fig. S7). This value is consistent with the expected diameter of individual crystallites observed from the discretisation of the width distribution at specific values (visible when plotting the experimental histograms in finer detail).

The effective 3D aspect ratio as calculated using **eq. 2** decreases with sonication dose (**Fig. 2F**). These aspect ratio values are smaller than those sometimes reported in the nanocellulose literature, perhaps due to differing definitions of the particle aspect ratio (e.g. $\alpha' = \frac{L_b}{T} \gg \alpha_{\text{eff}}$) (22). However, the relevance of the effective aspect ratio given by **eq. 2** is highlighted by its ability to predict CNC ensemble properties such as their hydrodynamic diameter (fig. S8).

As illustrated by **Fig. 1B-1D**, sonication breaks apart irregular CNC particles (bundles of crystallites) into simpler and more acicular sub-units (crystallites). The change in particle morphology can be quantified by size-invariant shape parameters such as particle rectangularity, defined by

$$R = \frac{A}{L_b W_b} = \frac{W_{\text{eq}}}{W_b} \quad (3)$$

The rectangularity ranges from 0 to 1, with 1 indicating an ideal rectangular particle. **Fig. 2G** clearly shows that sonication increases the mean particle rectangularity, providing a robust statistical evidence that CNCs are primarily fragmented by the lateral breaking of bundles. Further evidence can be readily obtained from other shape parameters, such as particle convexity and solidity (fig. S6).

Explaining chiral self-assembly behaviour from the CNC morphology

The statistical information provided by the morphological analysis offers insights into the self-assembly of CNCs.

The helicoidal configuration of CNC photonic films arises from their colloidal liquid crystalline ordering in suspension. At low volume fraction (<2 vol%) CNC suspensions are isotropic (I), while at higher volume fraction a lyotropic chiral nematic (N*) phase emerges due to the elongated shape of individual CNC particles (7). At intermediate volume fraction, the suspension is biphasic, with coexisting anisotropic and isotropic phases that can macroscopically segregate over time due to their different densities, as exemplified in **Fig. 3A**.

The equilibration of the structure is inhibited at high volume fraction (>10 vol%) by kinetic arrest (K.A.), where the crowding of the particles prevents further self-assembly into the chiral nematic phase. The nature of the kinetically-arrested structure (i.e. repulsive glass or attractive gel) depends on the colloidal interactions between the particles (8).

To clarify how the CNC self-assembly is affected by their morphology, we investigated the equilibrium phase diagram of CNC suspensions prepared at a range of concentration and sonication doses by allowing them to self-assemble in sealed capillaries (**Fig. 3B**, see Materials and Methods). The isotropic-biphasic boundary, easily made visible between cross-polarisers (**Fig. 3A**), appeared above a critical CNC volume fraction (ϕ_0) that was constant with sonication dose, whereas the biphasic-anisotropic boundary volume fraction (ϕ_1) increased with sonication dose. At high dose, sonication also advanced the kinetic arrest transition, with the low ionic strength of the suspensions and microscale appearance consistent with a repulsive Wigner glass.

In the biphasic region ($\phi_0 < \phi < \phi_1$), the relative proportion of the cholesteric phase determined from capillaries (**Fig. 3A**) increased gradually with the CNC volume fraction (**Fig. 3C**). At the highest dose (12 kJ/mL) a fully anisotropic state was not reached due to early kinetic arrest.

The phase behaviour of ideal hard colloidal rods is primarily determined by their aspect ratio, as shown by Onsager and subsequent authors (21, 23). For a suspension of identical hard cylindrical particles, the biphasic midpoint and biphasic width are inversely proportional to the cylinder aspect ratio:

$$\phi_m = \frac{c_m}{\alpha} \quad (4)$$

$$\Delta\phi = \frac{c_w}{\alpha} \quad (5)$$

where c_m and c_w are constants that depend on the specific particle model and trial function used to numerically solve coexistence equation: for instance, $(c_m, c_w) \approx (3.9, 1.2)$ in ref. (21).

The biphasic midpoint was found to be inversely proportional to effective 3D aspect ratio (**Fig. 2G**), in agreement with the scaling expected from **eq. 4**. The difference in c_m between CNCs ($c_m \approx 0.5$) and the idealised hard-rod model ($c_m \approx 4$) can be ascribed to electrostatic screening between CNCs, which leads to an effective particle volume fraction that is much greater than the experimentally measured (bare) volume fraction. In contrast, the biphasic width $\Delta\phi$ is greater than predicted ($\Delta\phi/\phi_m \approx 0.6$ for CNCs versus $\frac{\Delta\phi}{\phi_m} \approx 0.3$ for the ideal case) and showed no clear trend with aspect ratio, which can be attributed to the considerable polydispersity in particle aspect ratio. Nematic assembly of polydisperse rods has been shown to have much greater biphasic width and can lead to more complex phase separation behaviour (24, 25).

Beyond providing insights into the CNC phase diagram in suspension, the same sealed capillaries can also be used to investigate the chiral interactions between CNCs by measuring the cholesteric pitch for various sonication doses and CNC volume fraction. The pitch appears as twice the periodicity of the fingerprint pattern, characteristic of cholesteric phases and easily observed in polarised optical microscopy between cross-polarisers (**Fig. 3E**). At comparable CNC concentrations, a larger pitch is systematically observed for higher sonication doses, and this pitch difference between doses seems to be preserved as the samples are concentrated (**Fig. 3F**), suggesting that the red-shift observed in dried films originates from a larger pitch at low concentration. The chiral nematic wavevector $q = 2\pi/P$ appears to scale linearly with the CNC volume fraction ϕ :

$$q = \kappa\phi \quad (6)$$

where κ is a dose-dependent parameter, referred to as the chiral strength in this work, which captures the strength of the chiral interactions. The scaling behaviour in **eq. 6** agrees with the predicted behaviour for weakly chiral rods, while the scaling for strongly chiral rods is non-linear and is highly sensitive to particle shape (26, 27).

Expressing the mesophase chirality in terms of chiral strength instead of pitch enables direct comparison between values at a wide range of concentrations (**Fig. 3G**), which confirms that the chiral strength decreases with sonication dose.

Remarkably, the pitch scaling in **eq. 6** is reminiscent of the behaviour of chiral doping in molecular liquid crystals. For a nematic liquid crystal doped by chiral molecules at a concentration ϕ_d , the cholesteric wavevector of the resulting chiral nematic phase is

$$q = \frac{2\pi}{P} = 4\pi\beta_\phi\phi_d \quad (7)$$

where β_ϕ is the helical twisting power (per volume fraction of chiral dopants) (28). The scaling of the pitch seen in CNC suspension is therefore consistent with only a small proportion of the CNC population actively contributing to the mesophase chirality. Since the chiral strength decreases with sonication, which also breaks apart bundles, we hypothesised that the CNC bundles are acting as chiral enhancers, while individual CNC crystallites are effectively achiral and tend to form a (non-chiral) nematic phase.

To validate this hypothesis, it is useful to explore a physical system where the CNC concentration is kept fixed while the amount of bundles is varied. Such a system was achieved by simply mixing CNC suspensions of different doses at equal CNC volume fraction. A “low-dose” (772 J/mL) and “high-dose” (3072 J/mL) sample were chosen because their average particle size parameters are very similar while their cholesteric pitch at 12 wt% are substantially different ($p_{HI}/p_{LO} > 3$). Importantly, both suspensions were fully anisotropic at that range of concentration, ruling out any possible complications due to fractionation (29, 30). If the cholesteric pitch arises from general suspension properties (such as ionic strength), we could expect the pitches of the mixtures to be a simple linear interpolation of the pitches for the two original samples. In contrast, the chiral dopant model based on **eq. 7** predicts a harmonic pitch average for mixing (*i.e.*, a linear mixing in terms of the corresponding cholesteric wavevector q), due to variation of the abundance of bundles.

Fig. 3H shows the equilibrium pitch for mixtures of the low and high dose samples at various volumetric mixing ratios. The experimental data clearly follow the harmonic pitch average for the pitch, as expected for the chiral dopant hypothesis. Our findings should be compared with the results of (18), where a linear interpolation was found to be satisfactory to describe the pitch of CNC mixtures. This conclusion can be attributed to the small difference between the limiting values used in that work ($p_{HI}/p_{LO} \approx 1.5$), making linear interpolation in pitch or in inverse pitch very similar (*i.e.*, within 4% difference).

Relating the CNC mesophase chirality to the abundance of crystallite bundles

The evolution of the pitch in CNC mixtures reported in **Fig. 3** motivated us to re-examine the CNC shape analysis for evidence of a sub-population that acts as chiral dopants. However, the statistical analysis of CNC size and shape presents a complex picture of the evolution of the particle population with increasing sonication dose.

For instance, in **Fig. 2G** a low rectangularity (R) tail was observed at low dose, which disappeared at intermediate doses but re-emerged at high doses. Direct inspection of TEM images revealed that low-dose suspensions (≤ 48 J/mL) contained irregular particles of low rectangularity (*i.e.*, their shapes were poorly approximated by a bounding rectangle). The proportion of these irregular aggregates decreased as the sonication dose increased. In contrast, much high doses (≥ 771 J/mL) led to the emergence of kinked CNC particles, analogously to previously reports on CNCs extracted from tunicate or when sonicating cellulose nanofibers (20, 22). While these distorted or kinked objects also showed low rectangularity (due to the large bounding area), they looked rather like mechanically damaged individual crystallites, much different from the aggregate-like objects observed at lower doses.

From consideration of individual particle morphology, CNCs can be classified into different sub-populations according to their AE width and rectangularity, with threshold boundaries defined at $W_{eq} = 17$ nm and $R = 0.40$. The width threshold was chosen so that particles above this threshold are unquestionably bundles (*i.e.* with a width at least two times crystallite width), while the rectangularity threshold was chosen based on the shape of the distributions in **Fig. 2G**. The four resulting quadrants can then be considered to be representative of (1) Aggregates (W_{eq} high, R low), (2) Bundles (W_{eq} high, R high), (3) Crystallites (W_{eq} low, R high) and (4) Distorted (kinked) crystallites (W_{eq} low, R low).

Fig. 4A show CNC particle populations at various sonication doses are distributed between these four classes. The overall trend with sonication is an anti-clockwise migration from aggregates (bottom right) through bundles (top right) and crystallites (top left) to distorted crystallites (bottom left). Typical particles for each category are shown in **Fig. 4B**.

This proposed evolution of the CNC particle population with sonication is consistent with ensemble size measurements. At low dose, light scattering from the sample is dominated by aggregates and bundles, leading to high particle turbidity (fig. S4). Upon increasing the sonication dose, aggregates are readily converted into smaller structures, while the bundles are more persistent and require more energy to be converted into individual crystallites. At extreme sonication doses, a secondary process emerges where Crystallites become kinked, as evidence by the onset and growth of the distorted crystallite fraction.

This particle classification explains the non-trivial variation in hydrodynamic diameter with sonication, which decays rapidly at low sonication dose before steadily decreases at higher dose, apparently in a bi-exponential process (31). Moreover, it reveals that the low dose decay corresponds to the breakdown of aggregates, while the high dose decay corresponds to the more gradual breakdown of bundles.

The classification in **Fig. 4A-4B** can be used to explicitly calculate the relative volume fraction of each particle class within the CNC suspension, as shown in **Fig. 4C**. Comparing **eq 6** and **eq 7**, the dopant concentration can be related to the total CNC concentration by

$$\phi_d = \chi\phi \quad (8)$$

where χ is the relative dopant volume fraction within the nanoparticle population. We identify the aggregates and bundles as potential chiral dopants that contribute to χ .

The chiral strength shows a clear positive trend with dopant abundance, as shown in **Fig. 4D**. The chiral strength κ increases linearly with χ at low bundle abundance, in accordance with **eq. 7**, implying a constant helical twisting power at high sonication dose. At high dopant concentration, we observe saturation in the chiral strength due to non-linear interactions between dopants and non-dopants, similar to previous reports (4). Notably, the chiral nematic wavevector q tends to zero at high sonication, suggesting that the Crystallites alone are insufficient to propagate a collective chiral interaction required to induce a cholesteric liquid crystal phase. The limiting behaviour of **Fig. 4C** gives an estimate of the helical twisting power of $\beta_\phi = 4 \mu\text{m}^{-1}$, which is comparable to values obtained for DNA origami filaments and amyloid fibrils ($\beta_\phi \approx 2$ and $20 \mu\text{m}^{-1}$ respectively) (4, 5).

Discussion

In this work, tip sonication with high-intensity ultrasound was used to investigate the role of CNC morphology, characterised by TEM, on the chiral self-assembly of CNCs observed in suspensions and in films. By performing a detailed and statistically robust shape particle analysis, and relating it to quantitative analysis of their chiral behaviour, the crystallite bundle subpopulation within the CNC suspension was shown to be key for the transfer of chirality across length-scales.

These results point the way towards a new direction for CNC research. There is considerable variation in the morphology of CNCs when comparing different biological sources and extraction methods, which suggests that these factors determine the occurrence of CNC bundles. Conversely, the presence of bundles may partly explain differences in colloidal behaviour between CNCs prepared by different protocols. However, the precise origin of CNC bundles and their role in CNC colloidal self-assembly are yet to be explored in great detail.

These results also prompts a re-examination of previous results in light of this new understanding. For instance, CNC bundles provides a mechanism for the observed relationship between length and pitch found in recent work on fractionation of CNCs: as bundles have a higher 3D aspect ratio than crystallites, they phase-separate more easily than crystallites into the anisotropic phase (29, 30).

Standardising the characterisation of nanoparticle morphology is a major outstanding challenge for nanomaterials research (32, 33). The particle analysis developed for this study is widely transposable to other systems and may help address this challenge. For cellulose nanomaterials in particular, the discovered link between CNC morphology and their resulting chiral nematic properties makes a refined shape metrology particularly relevant for manufacturers tailoring their production for applications involving chiral self-assembly.

The role of bundles as chiral enhancers appears as a direct colloidal equivalent to the molecular chiral dopants routinely used in molecular liquid crystals. This paradigm distinguishes CNCs from other chiral colloidal systems and warrants further investigation as an efficient approach to producing large-scale self-organised chiral architectures using a small proportion of chiral seed particles.

Materials and Methods

Preparation of CNCs suspensions

Cellulose nanocrystals were obtained by acid hydrolysis of Whatman No. 1 cellulose filter paper (60 g) with sulfuric acid (64 wt%) at 64°C under high mechanical stirring. The reaction was quenched after 30 min by dilution of the acid with deionized ice and water and immersion of the reaction vessel in an ice bath. Soluble cellulose residues and excess acid were removed by three rounds of centrifugation at 20,000g (30, 20, 20 min respectively) with the pellet re-dispersed in deionized water after each round. Excess ions were removed by dialysis against deionized water using MWCO 12-14 kDa membranes. This purification resulted in a 2.43 wt% CNC suspension, which was used as the starting batch for further treatment.

Ultrasonication

The nanocrystal size was controlled by high-intensity sonication (Fisherbrand Ultrasonic disintegrator, 20 kHz, tip diameter 12.7 mm, 2:1 ON:OFF cycles). Unless otherwise stated, samples were sonicated at 2.0 wt% CNC with a sample volume of 20 mL in a modified centrifuge tube (Corning Falcon 50 mL), with the sonicator tip immersed to a depth of one-third of the sample volume. Samples were immersed in an ice bath throughout sonication to prevent sample heating, as de-sulfation of the CNCs surface charges has been observed in acidic suspensions at high temperatures (34). For longer sonication treatments, the ice bath was replenished every five minutes.

Dynamic light scattering (DLS)

DLS samples were prepared with CNC (0.1 wt%) suspended in 1 mM NaCl solution, and passed through a 0.8 μm cellulose acetate syringe filter before pouring into disposable plastic cuvettes. DLS measurements were performed with a commercial setup (Malvern Zetasizer Nano ZS) using 633 nm illumination and collecting back-scattered (173°) light. Samples were measured at 25°C after a delay of 300 s to allow for thermal equilibration before data collection, which was performed in three runs of at least ten measurements per run.

Transmission electron microscopy

TEM samples were prepared by casting a droplet of 0.001 wt% CNC suspension in pH 3 solution onto carbon-coated copper grid prepared by glow discharge and staining with uranyl acetate solution. TEM images were captured using a Talos F200X G2 microscope (FEI) operating at 200 kV and a CCD camera.

The CNC outlines were traced in Fiji and analysed using the Shape Filter plug-in. As CNCs exhibit considerable size polydispersity (for instance, the length polydispersity $\sigma_L/\mu_L \approx 0.5$), at least 250 particles were measured for each sample to ensure reliable statistics. A discussion of the tracing protocol is given in the Supplementary Information.

Preparation of CNC photonic films

To standardise the CNC suspensions after dialysis and ensure optimal visual appearance of the final films, each suspension was diluted to 1.60 wt% CNC in 1.92 mM NaCl solution. Films were cast from 2.5 mL of each suspension into a 35 mm diameter polystyrene Petri dish and left to dry under ambient conditions, which typically took 36 hours.

Polarised optical microscopy of CNC photonic films

Optical microscopy was performed on a Zeiss Axio microscope, with a halogen lamp (Zeiss HAL100) as light source using Koehler illumination. Images were captured in bright field reflection mode using a 10x objective (Nikon T Plan SLWD, NA 0.2) and recorded using CCD camera (UI-3580LE-C-HQ, IDS). The white balance of the images was calibrated using a white Lambertian diffuser.

Chiral nematic phase and pitch measurement.

CNC suspensions at a range of concentrations were prepared by first concentrating the stock using a rotary evaporator (40 °C, < 40 mbar), then diluted to the desired final concentration using deionized water.

Chiral nematic phase separation was observed in CNC suspensions at a range of concentrations. Glass capillaries were filled with the suspensions and sealed with UV epoxy (NOA 81), then left to equilibrate for at least two weeks. The anisotropic phase fraction was determined from the proportion of the suspension that appeared bright when viewed between crossed polarizers. The chiral nematic pitch of the anisotropic phase was measured from microscope images taken using a Zeiss Axioscope under transmission illumination with crossed polarizers.

References

1. W. Jiang, Z. Qu, P. Kumar, D. Vecchio, Y. Wang, Y. Ma, J. H. Bahng, K. Bernardino, W. R. Gomes, F. M. Colombari, A. Lozada-Blanco, M. Veksler, E. Marino, A. Simon, C. Murray, S. R. Muniz, A. F. de Moura, N. A. Kotov, Emergence of complexity in hierarchically organized chiral particles. *Science*. **368**, 642–648 (2020).
2. M. Y. B. Zion, X. He, C. C. Maass, R. Sha, N. C. Seeman, P. M. Chaikin, Self-assembled three-dimensional chiral colloidal architecture. *Science*. **358**, 633–636 (2017).
3. F. Tombolato, A. Ferrarini, E. Grelet, Chiral Nematic Phase of Suspensions of Rodlike Viruses: Left-Handed Phase Helicity from a Right-Handed Molecular Helix. *Phys. Rev. Lett.* **96**, 258302 (2006).
4. M. Siavashpouri, C. H. Wachauf, M. J. Zakhary, F. Praetorius, H. Dietz, Z. Dogic, Molecular engineering of chiral colloidal liquid crystals using DNA origami. *Nature Materials*. **16**, 849–856 (2017).
5. G. Nyström, M. Arcari, R. Mezzenga, Confinement-induced liquid crystalline transitions in amyloid fibril cholesteric tactoids. *Nature Nanotechnology*. **13**, 330 (2018).
6. M. M. C. Tortora, G. Mishra, D. Prešern, J. P. K. Doye, Chiral shape fluctuations and the origin of chirality in cholesteric phases of DNA origamis. *Science Advances*. **6**, eaaw8331 (2020).
7. J.-F. Revol, H. Bradford, J. Giasson, R. H. Marchessault, D. G. Gray, Helicoidal self-ordering of cellulose microfibrils in aqueous suspension. *International Journal of Biological Macromolecules*. **14**, 170–172 (1992).
8. R. M. Parker, G. Guidetti, C. A. Williams, T. Zhao, A. Narkevicius, S. Vignolini, B. Frka-Petesic, The Self-Assembly of Cellulose Nanocrystals: Hierarchical Design of Visual Appearance. *Advanced Materials*. **30**, 1704477 (2017).
9. C. Schütz, J. R. Bruckner, C. Honorato-Rios, Z. Tosheva, M. Anyfantakis, J. P. F. Lagerwall, From Equilibrium Liquid Crystal Formation and Kinetic Arrest to Photonic Bandgap Films Using Suspensions of Cellulose Nanocrystals. *Crystals*. **10**, 199 (2020).
10. K. E. Shopsowitz, H. Qi, W. Y. Hamad, M. J. MacLachlan, Free-standing mesoporous silica films with tunable chiral nematic structures. *Nature*. **468**, 422–425 (2010).
11. S. J. Hanley, J.-F. Revol, L. Godbout, D. G. Gray, Atomic force microscopy and transmission electron microscopy of cellulose from *Micrasterias denticulata*; evidence for a chiral helical microfibril twist. *Cellulose*. **4**, 209–220 (1997).
12. M. Khandelwal, A. Windle, Origin of chiral interactions in cellulose supra-molecular microfibrils. *Carbohydrate Polymers*. **106**, 128–131 (2014).
13. I. Usov, G. Nyström, J. Adamcik, S. Handschin, C. Schütz, A. Fall, L. Bergström, R. Mezzenga, Understanding nanocellulose chirality and structure–properties relationship at the single fibril level. *Nat Commun*. **6**, 7564 (2015).
14. X. M. Dong, T. Kimura, J.-F. Revol, D. G. Gray, Effects of Ionic Strength on the Isotropic-Chiral Nematic Phase Transition of Suspensions of Cellulose Crystallites. *Langmuir*. **12**, 2076–2082 (1996).
15. X. M. Dong, J.-F. Revol, D. G. Gray, Effect of microcrystallite preparation conditions on the formation of colloid crystals of cellulose. *Cellulose*. **5**, 19–32 (1998).

16. J. R. Bruckner, A. Kuhnhold, C. Honorato-Rios, T. Schilling, J. P. F. Lagerwall, Enhancing Self-Assembly in Cellulose Nanocrystal Suspensions Using High-Permittivity Solvents. *Langmuir*. **32**, 9854–9862 (2016).
17. J.-F. Revol, J. Godbout, D. G. Gray, Solid self-assembled films of cellulose with chiral nematic order and optically variable properties. *J. Pulp Paper Sci.* **24**, 146–149 (1998).
18. S. Beck, J. Bouchard, R. Berry, Controlling the Reflection Wavelength of Iridescent Solid Films of Nanocrystalline Cellulose. *Biomacromolecules*. **12**, 167–172 (2011).
19. L. Heux, G. Chauve, C. Bonini, Nonflocculating and chiral-nematic self-ordering of cellulose microcrystals suspensions in nonpolar solvents. *Langmuir*. **16**, 8210–8212 (2000).
20. S. Elazzouzi-Hafraoui, Y. Nishiyama, J.-L. Putaux, L. Heux, F. Dubreuil, C. Rochas, The Shape and Size Distribution of Crystalline Nanoparticles Prepared by Acid Hydrolysis of Native Cellulose. *Biomacromolecules* (2007), doi:10.1021/bm700769p.
21. L. Onsager, The Effects of Shape on the Interaction of Colloidal Particles. *Annals of the New York Academy of Sciences*. **51**, 627–659 (1949).
22. G. Nyström, M. Arcari, J. Adamcik, I. Usov, R. Mezzenga, Nanocellulose Fragmentation Mechanisms and Inversion of Chirality from the Single Particle to the Cholesteric Phase. *ACS Nano*. **12**, 5141–5148 (2018).
23. A. Stroobants, H. N. W. Lekkerkerker, T. Odijk, Effect of electrostatic interaction on the liquid crystal phase transition in solutions of rodlike polyelectrolytes. *Macromolecules*. **19**, 2232–2238 (1986).
24. H. H. Wensink, G. J. Vroege, Isotropic–nematic phase behavior of length-polydisperse hard rods. *J. Chem. Phys.* **119**, 6868–6882 (2003).
25. P. A. Buining, A. P. Philipse, H. N. W. Lekkerkerker, Phase behavior of aqueous dispersions of colloidal boehmite rods. *Langmuir*. **10**, 2106–2114 (1994).
26. J. P. Straley, Theory of piezoelectricity in nematic liquid crystals, and of the cholesteric ordering. *Phys. Rev. A*. **14**, 1835–1841 (1976).
27. S. Dussi, S. Belli, R. van Roij, M. Dijkstra, Cholesterics of colloidal helices: Predicting the macroscopic pitch from the particle shape and thermodynamic state. *The Journal of Chemical Physics*. **142**, 074905 (2015).
28. P. G. de Gennes, J. Prost, *The Physics of Liquid Crystals* (Clarendon Press, 1995).
29. C. Honorato-Rios, C. Lehr, C. Schutz, R. Sanctuary, M. A. Osipov, J. Baller, J. P. F. Lagerwall, Fractionation of cellulose nanocrystals: enhancing liquid crystal ordering without promoting gelation. *NPG Asia Materials*, 1 (2018).
30. C. Honorato-Rios, J. P. F. Lagerwall, Interrogating helical nanorod self-assembly with fractionated cellulose nanocrystal suspensions. *Communications Materials*. **1**, 1–11 (2020).
31. A. Brinkmann, M. Chen, M. Couillard, Z. J. Jakubek, T. Leng, L. J. Johnston, Correlating Cellulose Nanocrystal Particle Size and Surface Area. *Langmuir*. **32**, 6105–6114 (2016).
32. M. Calvaresi, The route towards nanoparticle shape metrology. *Nat. Nanotechnol.* **15**, 512–513 (2020).

33. L. Boselli, H. Lopez, W. Zhang, Q. Cai, V. A. Giannone, J. Li, A. Moura, J. M. de Araujo, J. Cookman, V. Castagnola, Y. Yan, K. A. Dawson, Classification and biological identity of complex nano shapes. *Communications Materials*. **1**, 1–12 (2020).
34. Beck, Auto-catalyzed acidic desulfation of cellulose nanocrystals. *Nordic Pulp and Paper Research Journal*. **29**, 006–014 (2014).

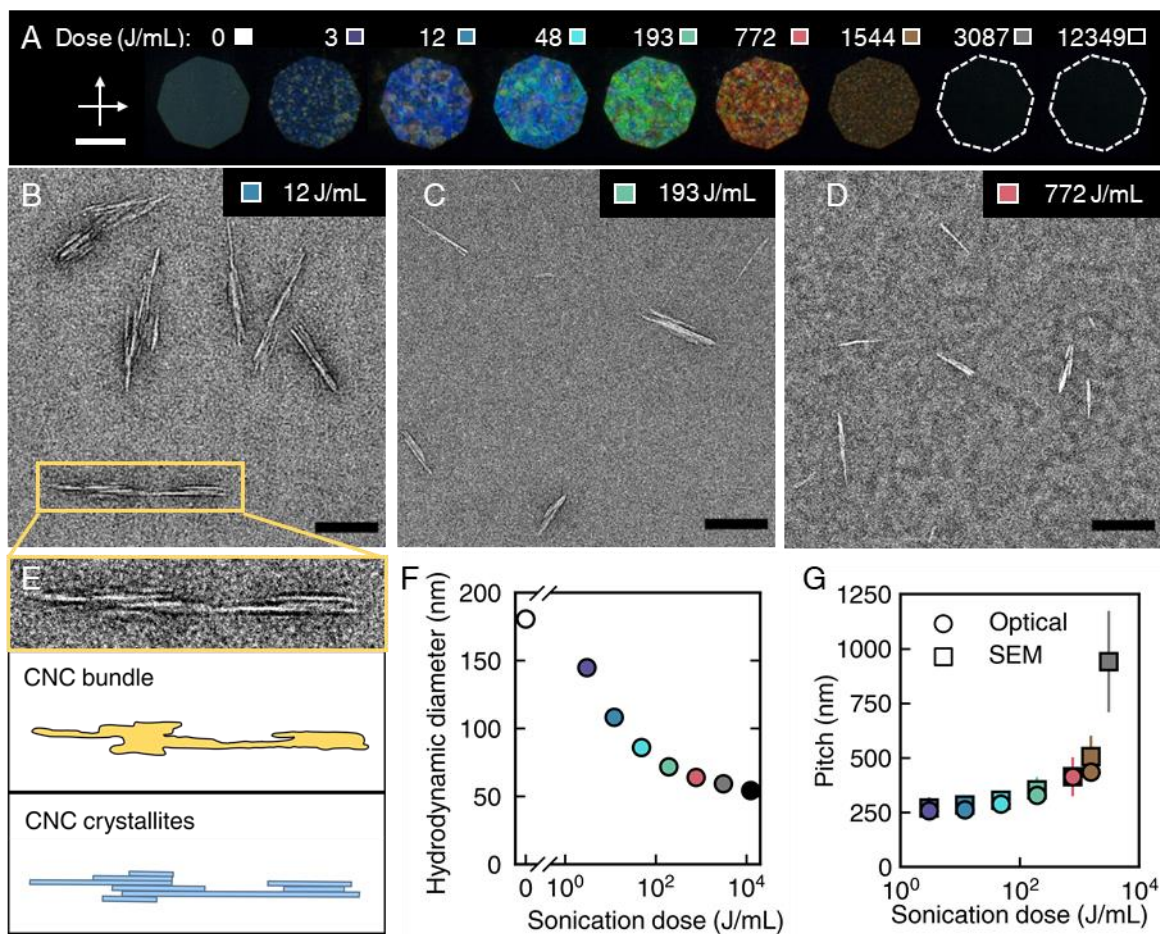


Figure 1 Tuning the colour of CNC photonic films with sonication (A) CNC photonic films of increasing sonication dose viewed under crossed polarisers. Square panel next to each dose value indicates the colour code used for other plots. Scale bar 100 μm . (B-D) TEM images of CNCs corresponding to blue (B), green (C) and red (D) photonic films. Scale bar 200 nm. (E) Example of a CNC bundle from (B). Scale bar 50 nm. Blue rectangles indicate composition of the bundle from elementary CNC crystallites. (F) Decrease in average hydrodynamic diameter (DLS z-average diameter) with sonication dose. (G) Pitch increase with sonication dose, as inferred from optical spectroscopy (fig. S2) and cross-sectional scanning electron microscopy (SEM, fig. S3).

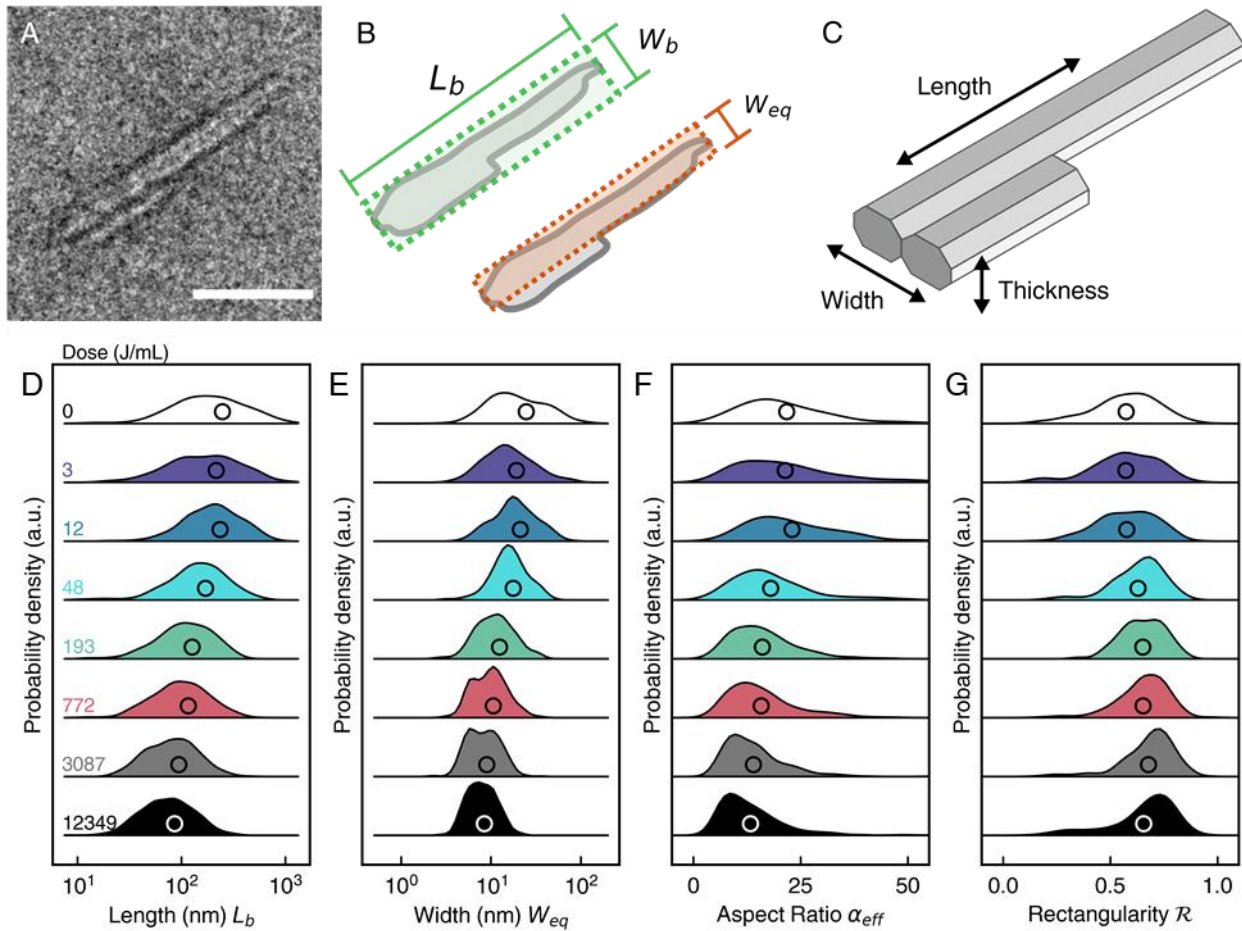


Figure 2 Revealing the 3D morphological changes due to sonication by nanoparticle shape metrology (A) Example of a CNC bundle in a TEM image. Scale bar 50 nm. (B) Definition of the box length, box width, and area-equivalent (AE) width. (C) Schematic of the 3D morphology of the particle in (A), with the length, width and thickness dimensions indicated (D-G) Distributions in particle size and shape parameters for box length (D), AE width (E), effective 3D aspect ratio (F) and rectangularity (G). Sonication dose indicated by the values on the left-hand size and plot colour. Circles indicate mean values.

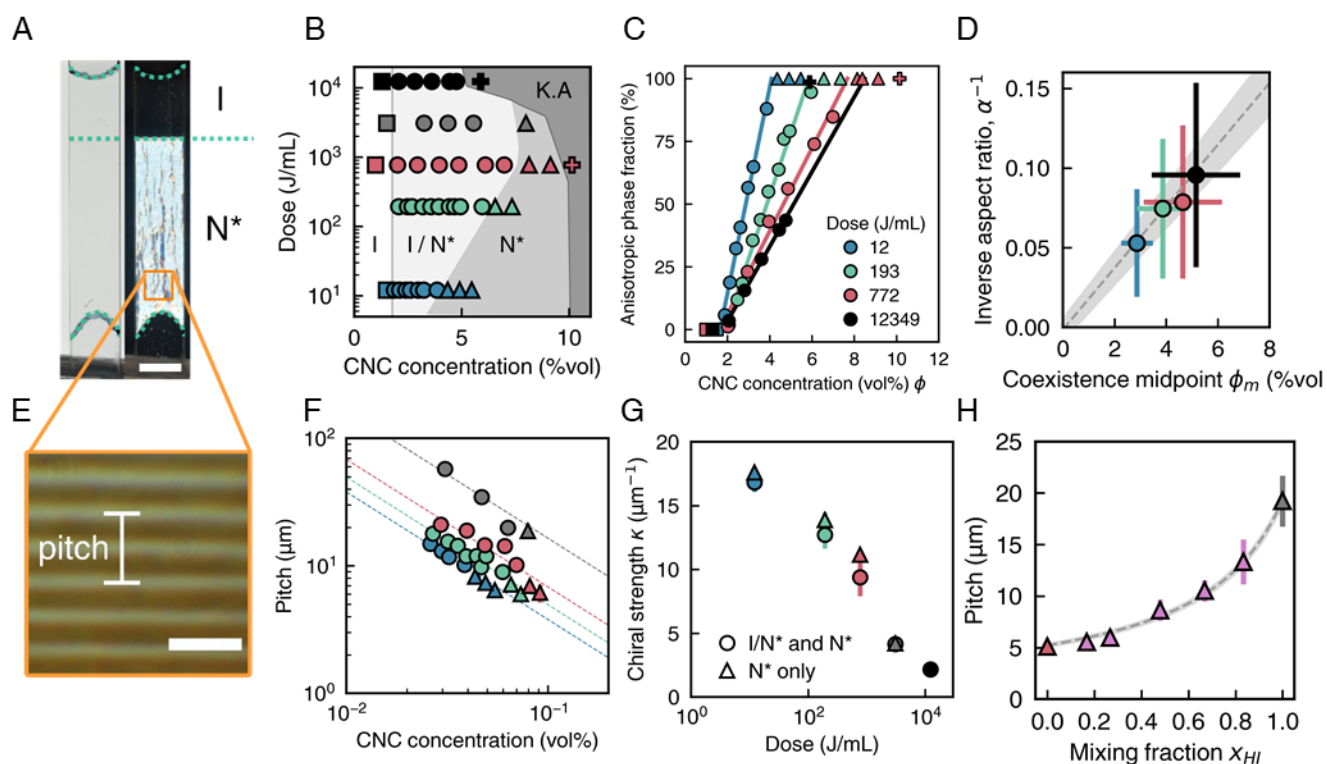


Figure 3 Explaining chiral self-assembly behaviour using CNC morphology (A) Macroscopic phase separation of a biphasic CNC suspension in a sealed rectangular glass capillary. Vertical separation into isotropic (I) and anisotropic chiral nematic (N^*) phases is evident when viewed under crossed polarisers (right photograph). Scale bar 5 mm (B) Phase diagram versus CNC concentration and sonication dose, with the isotropic (I, squares), biphasic (I/ N^* , circles), chiral nematic (N^* , triangles) and kinetically arrested (K.A., crosses) phases indicated. (C) Anisotropic (N^*) phase fraction versus concentration. Values determined using capillaries as exemplified in (A). (D) Midpoint of the biphasic region versus mean inverse aspect ratio (Figure 2g), demonstrating linear relation in accordance with Onsager theory for ideal hard rods. (E) Polarised optical microscopy of the N^* phase from (A). The fingerprint pattern characteristic of chiral nematic suspensions is observed and used to determine the pitch. Scale bar 10 μm . (F) Variation in pitch with CNC concentration for biphasic and chiral nematic suspensions (symbols match the phase diagram (B)). Dotted lines indicate fitting to equation 6 using I/ N^* and N^* pitch values. (G) Decrease in chiral strength κ with sonication dose. (H) Pitch of mixtures of “low” and “high” dose suspensions at equal CNC volume fraction. Grey line indicates fitting to chiral dopant model.

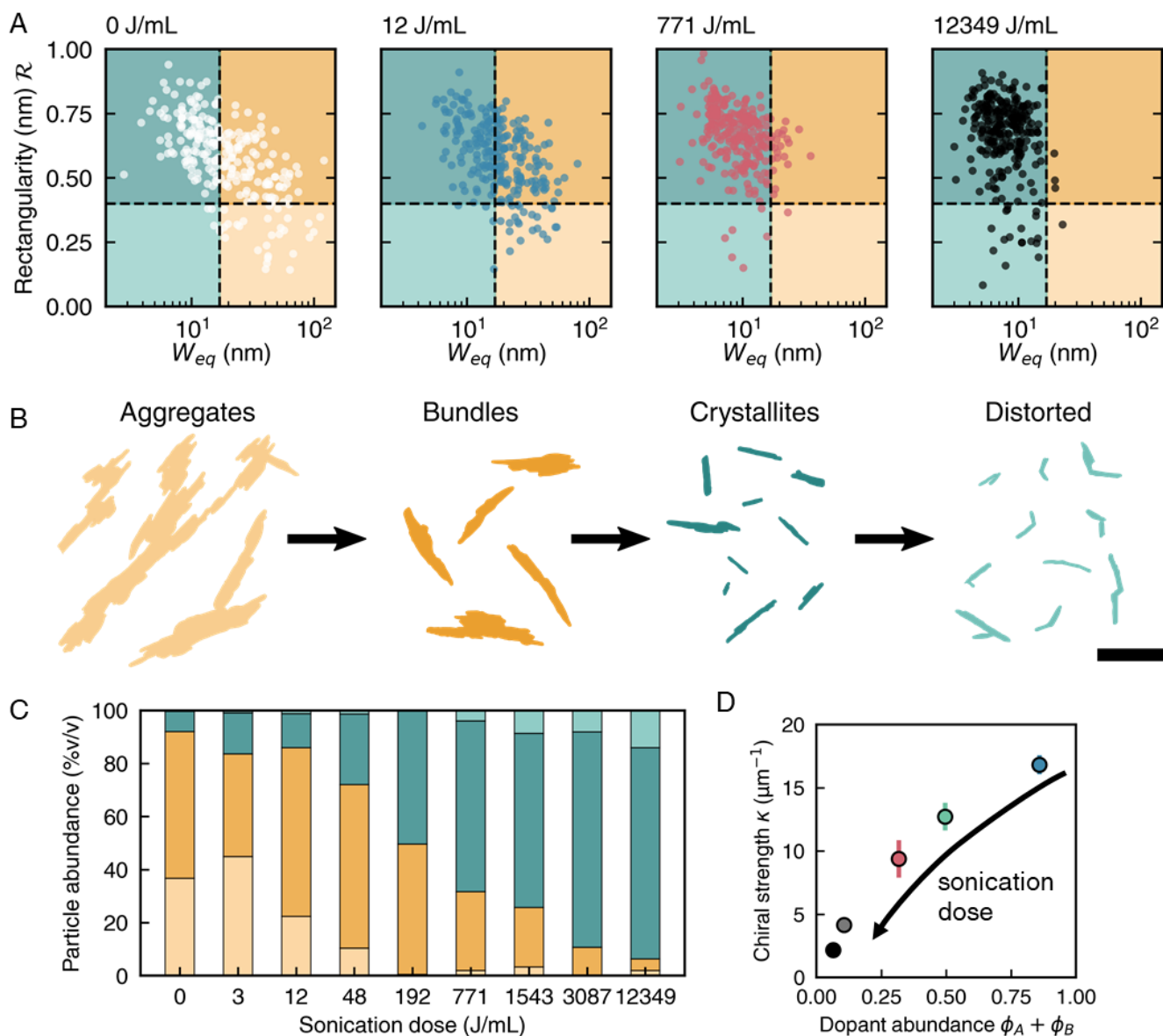


Figure 4 Relating the CNC mesophase chirality to the abundance of crystallite bundles (A) Classification of CNC particles into four categories based on AE width and rectangularity. Scatter plots of AE width versus rectangularity are shown for four sonication doses, illustrating the evolution of the system under sonication. (B) Representative examples of each particle category. Evolution under sonication indicated by black arrows. (C) Abundance of each particle class (expressed as relative volume fraction) for increasing sonication dose. (D) Chiral strength versus abundance of dopants (A and B particles).